Lund University,
Faculty of Engineering

Master Thesis

Neutron Reflectometry performed on an Iridium Sample using the Multi-Blade Detector

Author:
Alexander Backis

Supervisor:
Kevin Fissum

Co-Supervisor:
Francesco Messi

Lunds tekniska högskola
Lunds universitet

2018-05-30

Abstract

The current thesis presents the results from a neutron reflectometry analysis performed on data collected at ISIS in Rutherford Appleton Laboratories, England, in October 2017. The CRISP instrument was used and the Multi-Blade incorporated as a detector. This was the first attempt ever to use the Multi-Blade in this type of measurement. The Multi-Blade is a cold and thermal neutron detector currently in the prototype stage. It will eventually be used for reflectometry measurements at the European Spallation Source. The measurement was performed on a known $\sim$550 Å thick Iridium layer deposited on a Silicon substrate. In the thesis, the collected raw data were processed to form candidate neutron events. This was done by data reduction followed by clustering. A fitting procedure was then performed on the created candidate events. From this the thickness of the Iridium sample was correctly identified, with a fitting parameter found to be 550 Å $\pm$ 2.75 Å. This demonstrates the capabilities of the Multi-Blade detector to accurately identify thin samples. In the outlook it is discussed how to further increase the accuracy of this result. This can be done by utilising the high spatial resolution of the Multi-Blade detector.

Abbreviations

NREF	Neutron Reflectometry
MWPC	Multi Wire Proportional Chamber
SLD	Scattering Length Density
ESS	European Spallation Source
RAL	Rutherford Appleton Laboratories
ToF	Time-of-Flight

Preface

This thesis was written in a collaboration between the European Spallation Source (ESS) and Lund University. The work on the thesis was conducted at Lund University at the Division of Nuclear Physics, where office space was provided by the Sonnig group. The thesis is a part in the work of testing and developing the Multi-Blade detector, which upon completion will be installed at ESS. The purpose of the thesis was to analyse data collected with the Multi-Blade during measurements in october 2017 (three months before the work on the thesis began), and investigate if the detector can correctly identify the sample that was under study.

The entire experience have been fantastic. First of all, I want to thank all my co-workers in the Sonnig group for their warm welcome. I want especially to thank my supervisors Francesco Messi and Kevin Fissum for all their help, encouragement and support with my writing and taking their time to explain difficult concepts. I want to thank Francesco Piscitelli and Giacomo Mauri for introducing me to the Multi-Blade detector, and for many valuable discussions concerning the data analysis. Special thanks to Giacomo for many rewarding email conversations. I also want to thank Hanno Perry for taking his time and showing me good packages in Python, and encouraging me to write code in a clear and precise fashion.

A special thanks go out to all my friends, especially Sofie Karlsson and Jonathan Lindberg, who cared to listen to me about neutrons, the Multi-Blade and ESS, seemingly without end.

Contents

Chapter 1

Introduction

The neutron is a particle with highly interesting properties. It is an electromagnetically neutral particle, and therefore insensitive to electromagnetic charge. Instead, the neutron interactions are primarily through the nucleon-nucleon force [1], making neutrons effective in differentiating between isotopes of the same element [2]. Furthermore, the interactions and properties of the neutrons are highly energy-dependent. Because of this, neutrons are classified by their energy.

Two important categories of neutrons are those of *cold* and *thermal* energies. These have energies in the range $\sim$2 meV and $\sim$25 meV, respectively. Cold and thermal neutrons have sufficiently low energy to scatter elastically on surfaces, and are hence non-destructive. Consequently, when cold or thermal neutrons are used to probe a sample, it allows for coherent scattering between neutron waves reflected from different layers in the material to occur. This allows for interference patterns to emerge, which gives information about the internal structure of layers [3]. Whenever the word "neutron" appears in the present thesis, it is meant synonymous with cold or thermal neutron, unless otherwise specified.

Neutron reflectometry (NREF) uses the reflection of cold and thermal neutrons to study the characteristics of thin structures on the atomic scale [2]. It is implemented by sending a highly collimated neutron beam at a small incident angle towards a sample, and then measuring the fraction of reflected neutrons. The results can reveal information about the depth structure of the sample, illuminating internal structures invisible to other methods [4]. As NREF is non-destructive, it is excellent for delicate samples (such as biological materials). At the same time, due to the small length scale (order of a few angstrom), it is excellent for discerning fine details [5]. The method is used in studies of a wide range of applications, such as laundry detergents, corrosion, pharmaceutics, foams, and food technology, to name a few [5, 6, 7, 8]. This makes the method important in the development of many commercial products.

The main limitation of NREF is the availability of neutron flux. For low fluxes, the mea-

surement requires long irradiation times. Consequently, spallation sources are preferred, since these can provide the necessary flux. The higher flux also resultes i better signal-to-noise ratio. One new spallation source is the European Spallation Source (ESS) [9], currently under construction in Lund, Sweden. ESS will be an unprecedentedly powerful neutron source, due to its high neutron flux. As such, it will be an excellent location to perform NREF. Due to the high flux, the facility will require a new generation of detectors, with a higher counting rate capability, to fully utilise the potential of the beam. One of these new detectors is the Multi-Blade [10, 11].

The Multi-Blade is currently being developed in a collaboration between ESS, Lund University and the Wigner Research Center, and is financed by the European grant BrightnESS (grant number 676548). To detect neutrons, the Multi-Blade uses a thin Boron layer in a Multi Wire Proportional Chamber (MWPC) oriented with a specific geometry. Furthermore, the amplification factor in the gas chamber is kept very low. This is a concept resulting in unprecedented resolution and counting rate [11]. When the final version of the detector is completed, it will be installed in the FREIA [12] and ESTIA [13] instruments at ESS. As the detector is still in the prototype stage, the current prototype MB16 is undergoing rigorous testing. In October 2017, the first test on the MB16 prototype in a NREF instrument was conducted at Rutherford Appleton Laboratories (RAL), England [14]. In this thesis, the analysis of the NREF data collected from an Iridium sample is performed.

Specifically, a NREF analysis on data collected at ISIS, RAL, when the Multi-Blade was used in the CRISP reflectometry instrument is performed. The data were collected during measurements on a $\sim$550 Å thick Iridium layer, deposited on a Si substrate, with a roughness of approximately 10 Å between the interfaces [14]. Iridium was chosen for its well-documented properties, making it an excellent first sample to characterise the functionality of the detector. A well-defined reflectometry profile that can be clearly identified was anticipated. Consequently, if the sample is correctly characterised from the test data, it is a good indicator that the prototype is working as expected.

The thesis will start by presenting the theory concerning NREF (Chapter 2). Then, the ISIS facility and CRISP experimental hall will be discussed (Chapter 3.1.1 - 3.1.2). This is followed by a brief introduction of the Multi-Blade detector and how the measurement was performed (Chapter 3.1.3). After that, the procedure of the data analysis is examined, explaining the different steps of reduction, clustering and reflectometry analysis (Chapter 3.2). Finally the results are presented, where the aggregated reflectometry result from several different incident angles, ranging from 0.2° to 0.8°, are shown. A best fit is performed on the data to extract information about some of the sample parameters, such as the thickness of the Iridium layer. Finally, an outlook is presented with suggestions for further investigations concerning the clustering procedure and reflectometry analysis, explaining how the procedure can be improved to access more of the raw data and further enhance the accuracy of the results (Chapter 4.1).

Chapter 2

Neutron Reflectometry

NREF uses cold and thermal neutrons to probe materials by examining the reflection of the neutrons. It is performed by sending a beam of neutrons at a low glancing incident angle θ towards a sample, and studying how the neutrons are reflected. The measured property is the *reflectivity*, which is defined as the fraction of reflected neutrons. It depends on both the incident angle θ and the neutron wavelength λ_n, see Fig. 2.1 [2]. Consequently, a measurement of the reflectivity for a large dynamic range may be accomplished by varying either of these variables [6]. The reflectivity is usually presented as a function of the momentum transfer q_z, perpendicular to the sample surface. This quantity, which depends on both variables θ and λ_n, is defined as:

$$q_z = \frac{4\pi}{\lambda_n} \sin\theta \tag{2.1}$$

where λ_n is the neutron wavelength and θ is the incident angle on the sample. Using q_z as the variable facilitates the comparison between results from all types of measurements, λ_n- and θ-sweep or a combination of both. Furthermore, it allows for a larger spectrum of reflectivity to be presented, since data can be collected using several different θ-values from the same source, which likely have a fixed bandwidth in λ_n.

The theory in the thesis is based on the wave-particle duality, which states that neutrons can be regarded both as particles and waves [1].[1] To calculate the neutron wavelength, the De Broglie relation for a free neutron is used:

$$\lambda_n = \sqrt{\frac{h^2}{2E_n m_n}} \tag{2.2}$$

where is h Planck's constant, E_n the neutron energy, and m_n the neutron mass [1].

[1] While quantum mechanics and the neutron wave-function from the Schrödinger equation should in principle be employed, classical optics and the Fresnel equation are sufficient in this case.

However, as the neutron waves also have a direction, a wave vector may be introduced:

$$\boldsymbol{k} = k \cdot \hat{\boldsymbol{v}} = k \cdot \begin{bmatrix} \cos(\theta) \\ \sin(\theta) \end{bmatrix}, \quad k = \frac{2\pi}{\lambda_n}, \tag{2.3}$$

where $\hat{\boldsymbol{v}}$ is the unit vector in the direction of the wave, k is the wave number, and θ angle of incidence of the neutron with respect to the surface, see Fig. 2.1. Using this formalism, the Fresnel equations may be applied to investigate the behaviour of neutrons incident on a single and double interface.

2.1 Theory

Three main wave concepts are highly relevant to NREF: *reflection*, *transmission*, and *interference*. These features are illustrated schematically in Fig. 2.1.

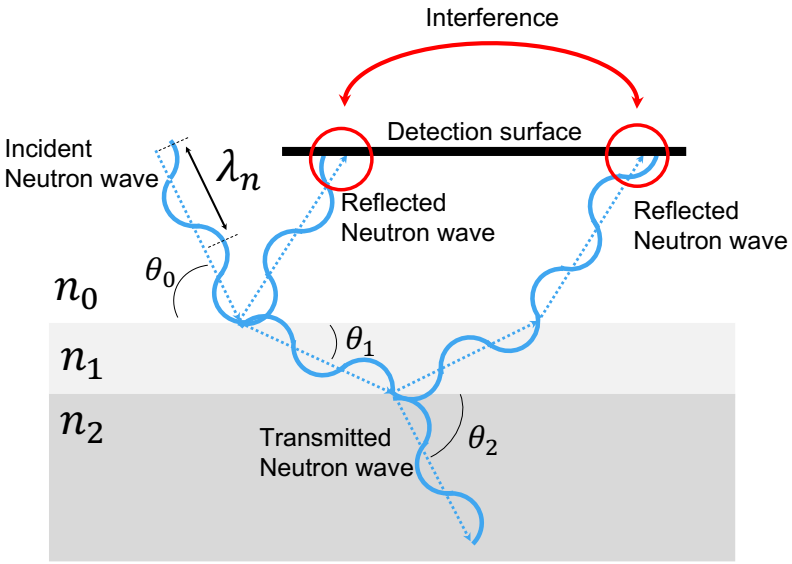

Figure 2.1: A schematic illustration of the concept of wave reflection, transmission and interference. A free neutron with wavelength λ_n is incident on a layered material with refractive indices n_1 and n_2. It is seen how the wave is reflected and transmitted, and how interference occurs at the detection surface.

When a neutron wave strikes the surface, it can be reflected or transmitted. Assuming elastic interactions, the angle of incidence is equal to the angle of reflection.[2] This

[2]The incident cold and thermal neutrons have insufficient energy to significantly move the atoms in the substrate; hence, the atoms can to a good approximation be considered stationary. Therefore, to preserve momentum, the reflected neutron is required to have the same velocity, with a reversed vertical direction, as the incident. Consequently, the reflected angle is required to be equal to the incident angle.

is called *specular* reflection. If there is more than one surface, interference can occur between the waves reflected from the different boundaries. As seen in Fig. 2.1, when the two reflected waves reach the detection surface there is a *phase shift* between them. This phase shift results from the path difference between the first and second reflected wave. In this case, the second wave travelled an additional distance of $2.5\lambda_n$, resulting in the first reflected wave being at the crest and the second at the trough when they reach the detection surface. The resultant wave is the superposition of the two waves, which in this special case is zero.

Thus, the behaviour of the reflected wave depends on the refractive index and the layered structure of the material. The refractive index determines how much the wave is refracted (that is, "bent" from the initial trajectory), and the layered structure determines the distance between the layers. Both these properties contribute to the resulting interference phenomena, since they determine the path difference between the first and second reflected wave. By probing a material with neutron waves and examining the resulting reflectivity pattern, these material properties can be discovered.[3] Furthermore, the refractive index can be determined according to:

$$n = \sqrt{1 - \frac{\lambda_n^2 N_b}{\pi}}, \tag{2.4}$$

where λ_n is the neutron wavelength and N_b the *Scattering Length Density* (SLD) [2], which is a property of the nuclei in the material. N_b differs between elements and isotopes of the same element. It is therefore sufficient to relate a material to a specific N_b instead of the refractive index n, and this is the convention used throughout the thesis.

[3]Note that the current method only probes in the depth direction of the material, and gives no information about in-plane properties of the samples under study.

2.1.1 Single interface

The physical situation in a neutron-reflectometry experiment, when studying a single-layer sample, can to first approximation be treated as a free-neutron wave incident on an infinitely thick interface where only elastic interactions are considered, see Fig. 2.2.

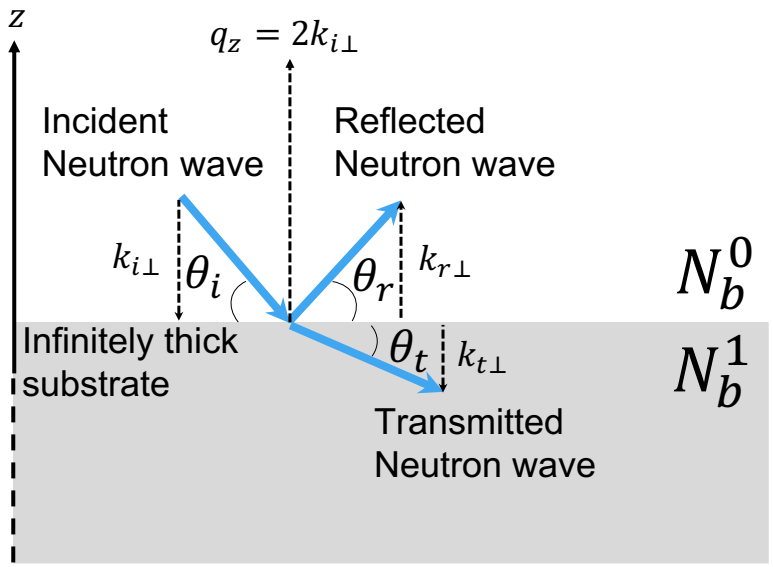

Figure 2.2: An schematic illustration of a neutron incident on an infinitely thick substrate, considering only elastic collisions. The neutron is represented as a wave vector (shown in blue), incident on the substrate (shown in grey) at a grazing angle θ_i. It is reflected at an angle θ_r, and transmitted with an angle θ_t. The normal components of the incident, reflected and transmitted wave vectors are represented as $k_{i\perp}$, $k_{r\perp}$ and $k_{t\perp}$, respectively. The momentum transfer in the normal direction (shown in dashed line) is labelled q_z.

The feature of interest in this situation is the fraction of reflected neutrons, which is calculated using the Fresnel coefficient for reflection:

$$r = \frac{k_{i\perp} - k_{t\perp}}{k_{i\perp} + k_{t\perp}}, \tag{2.5}$$

where $k_{i\perp}$ and $k_{t\perp}$ are the normal components of the incident and transmitted neutron wave vectors, respectively [2]. Using the incident angle and energy of the incoming neutron, $k_{i\perp}$ is calculated using Eqs. (2.2) and (2.3):

$$k_{i\perp} = \frac{2\pi}{\lambda_n} \cdot \sin\theta_i, \tag{2.6}$$

where λ_n is the wavelength of the incident neutron and θ_i is the incident angle. The calculation of $k_{t\perp}$ depends on both $k_{i\perp}$ and the incident material. Below a certain energy threshold, the incident neutron will have insufficient energy to be transmitted through

the substrate [2]. Consequently, $k_{t\perp} = 0$ at these energies, which is called the region of *total reflection*. $k_{t\perp}$ is thus:

$$k_{t\perp} = \begin{cases} 0, & k_{i\perp} \leq k_{i\perp}^c \\ \sqrt{k_{i\perp}^2 - (k_{i\perp}^c)^2}, & k_{i\perp} > k_{i\perp}^c \end{cases}, \tag{2.7}$$

where $k_{i\perp}^c$ is the *critical value* for which all incident neutrons with $k_{i\perp} \leq k_{i\perp}^c$ are reflected [2]. This value is a parameter dependent on the SLD of the substrate, and is found using:

$$k_{i\perp}^c = \sqrt{4\pi N_b}, \quad N_b = \sum_{i=0}^{N} b_i n_i. \tag{2.8}$$

N_b is the SLD of the substrate, n_i the number of nuclei per unit volume, b_i the scattering length of nucleus i, and N the number of different nuclei. The scattering length is a property of the target nucleus specifying the probability of the incident neutron to be scattered. By calculating the aggregated scattering length from all different nuclei in a material per unit volume, the SLD is determined. This is a parameter specifying the probability of a neutron scattering when travelling through the material [2].

Equation (2.5) may be rewritten to depend on q_z. This is preferable since q_z is the variable used when presenting results from measurements. Inserting Eq. (2.7) in (2.5) yields:

$$r = \frac{k_{i\perp} - \sqrt{k_{i\perp}^2 - (k_{i\perp}^c)^2}}{k_{i\perp} + \sqrt{k_{i\perp}^2 - (k_{i\perp}^c)^2}} = \frac{q - \sqrt{q^2 - q_c^2}}{q + \sqrt{q^2 - q_c^2}}, \tag{2.9}$$

where $q_z = 2k_{i\perp}$, giving the critical value:

$$q_c = 2k_{i\perp}^c = \sqrt{16\pi N_b}. \tag{2.10}$$

The reflectivity R is thus given by:

$$R = r^2 = \left| \frac{q - \sqrt{q^2 - q_c^2}}{q + \sqrt{q^2 - q_c^2}} \right|^2. \tag{2.11}$$

2.1.2 Double interface

The experimental situation in the present thesis involves the study of a thin film deposited on a substrate. In this approximation, it is assumed that the boundaries between the interfaces are rough, and that the substrate is infinitely thick, see Fig. 2.3.

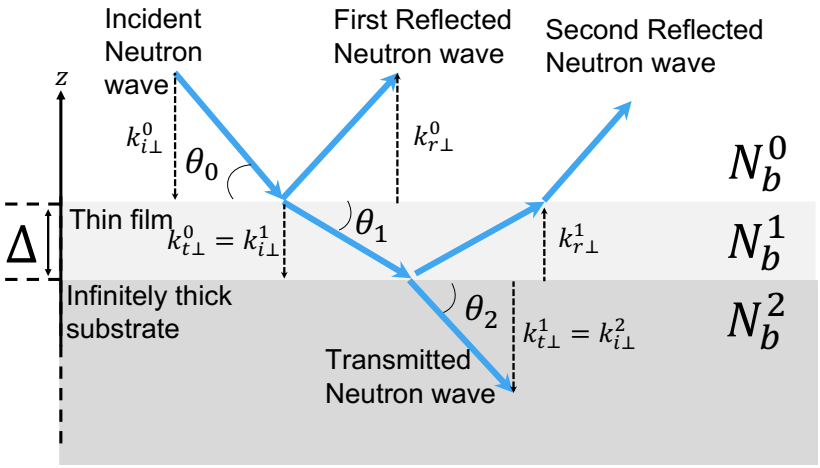

Figure 2.3: Schematic illustration of a thin film of thickness Δ deposited on an infinitely thick substrate. The angles θ_0, θ_1 and θ_2 are the angles of the incident neutrons with respect to the interface plane, while k_i^n, k_r^n and k_t^n are the normal components of the incident, reflected and transmitted wave vectors (shown in blue) in medium n, respectively. The different mediums are shown in white, light grey, and dark grey. These have the corresponding SLD values N_b^0, N_b^1 and N_b^2, respectively.

As there are two interfaces where the neutrons can reflect, this results in interference between neutron waves reflected at the top of the thin film and top of the substrate. The reflection r in this situation is:

$$r = \frac{r_0 + r_1 e^{ik^1_{i\perp} 2\Delta}}{1 + r_0 r_1 e^{ik^1_{i\perp} 2\Delta}}, \tag{2.12}$$

where Δ is the thickness of the film, $k^1_{i\perp}$ the perpendicular component of the incident wave vector inside the film, and r_0 and r_1 the reflection at the air-film interface and film-substrate interface, respectively [4]. The reflection r_n at an interface n is given by an expression similar to that for an infinitely thick substrate, recall Eq. (2.9), but modulated by an exponential to account for the roughness at each interface:

$$r_n = \frac{q_i^n - \sqrt{(q_i^n)^2 - (q_c^n)^2}}{q_i^n + \sqrt{(q_i^n)^2 - (q_c^n)^2}} e^{-0.5(q_i^n q_t^n < \sigma_n >)}, \tag{2.13}$$

where n is the interface of reflection, $q_i^n = 2k^n_{i\perp}$, $q_t^n = 2k^n_{t\perp}$, and $< \sigma_n >$ is the root mean square of the *roughness*, which is defined as the average thickness of irregularities between

the interfaces [4]. The roughness diffuse the neutron beam, reducing the intensity in the specular direction.[4] This affects the reflectivity profile, resulting in a faster decline for larger values of q_z [2].

Equation (2.12) and (2.13) result in the reflectivity for a thin layer:

$$R = r^2 = \left| \frac{r_0 + r_1 e^{ik_{i\perp}^1 2\Delta}}{1 + r_0 r_1 e^{ik_{i\perp}^1 2\Delta}} \right|^2 . \tag{2.14}$$

2.2 Profile

A visualisation of the reflectometry profile may be achieved by plotting the reflectivity as a function of the momentum transfer q_z. In Fig. 2.4, a double-interface reflectivity profile is presented as a function of q_z. This corresponds to the situation under investigation in the current thesis, where a thin film has been deposited on a thick substrate.

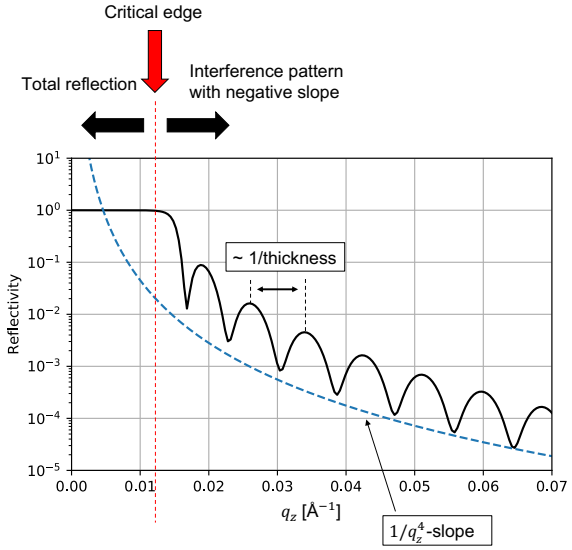

Figure 2.4: Schematic illustration presenting a typical specular neutron reflectometry curve from a film deposited on a substrate. The reflectivity profile (black curve) is plotted as a function of the momentum transfer q_z perpendicular to the interface. Under the red arrow is the critical edge (dotted red line) which separates the two regions. To the left of the critical edge is the region of total reflection. To the right of this edge is the region with fringes and decline. The fringes result from interference between neutron waves reflected at the sample surface and the substrate surface. The decline results from the diminishing probability of reflection. This decline tends towards $\propto \frac{1}{q_z^4}$ (dotted blue curve) for $q_z >> q_z^c$.

[4]This is because the irregularities are small "bumps" in the surface, which are not parallel to the rest of the surface. Therefore, when the neutron wave hits the bump, it will be reflected specularly with respect to the plane of the bump, not the rest of the surface.

The *critical edge* (red dotted line), is the q_z^c-value for which total reflection occurs for all $q_z \leq q_z^c$. The critical edge provides information about the SLD of the material under study, see Eq. (2.10).[5] Furthermore, since the SLD results from interactions with nuclei, information about the average distribution of nuclei in the material can be obtained. Since the interaction between nuclei can vary strongly as a function of isotope, neutrons may be used to probe subtle details that other probing methods, based on electromagnetic interactions, cannot discern.

Left of the critical edge, a plateau with value 1 is seen. This results from total reflection of the incident neutrons. To the right of the critical edge, an inference pattern is seen. This results from interference between neutron waves reflected from the sample surface and the substrate surface. From the distance between the fringes, information about the thickness of the sample material may be extracted. For $q_z >> q_z^c$, this is approximated according to:

$$\Delta \approx \frac{2\pi}{s} \tag{2.15}$$

where s is the spacing between the fringes and Δ the thickness of the layer [5]. This approximation of thickness, together with information about the critical edge, can be used to find starting parameters in the final fitting procedure. This is shown in Chapter 4.

There is also a clear fall in reflectivity in the curve right of the critical edge. This is primarily a consequence of the increasing fraction of transmitted neutrons with increasing incident neutron energy. However, it also depends on the roughnesses between each layer. A larger roughness between the interfaces results in the neutrons being diffused to a greater degree, decreasing the fraction of neutrons being reflected in the specular direction. Absorption also makes the curve fall off faster. Absorption lowers the number of reflected neutron, and can prevent the reflectivity to reach unity at total reflection [2].

[5] Note that the critical edge is often defined by the SLD of the substrate, not the sample. This is a consequence of the tunnelling effect, which allows the neutron, even though the kinetic energy is below the potential barrier of the sample, to penetrate a small distance and actually reach the substrate, where it is reflected [2].

2.3 Instrument

As described in Chapter 2.1, the measured feature in NREF is the reflectivity, which is presented as a function of q_z. Therefore, knowledge of the neutron reflectivity at a wavelength λ_n requires knowledge of both the number of incident and reflected neutrons. A schematic outline of a NREF instrument, and the measurement procedure, is presented in Fig. 2.5.

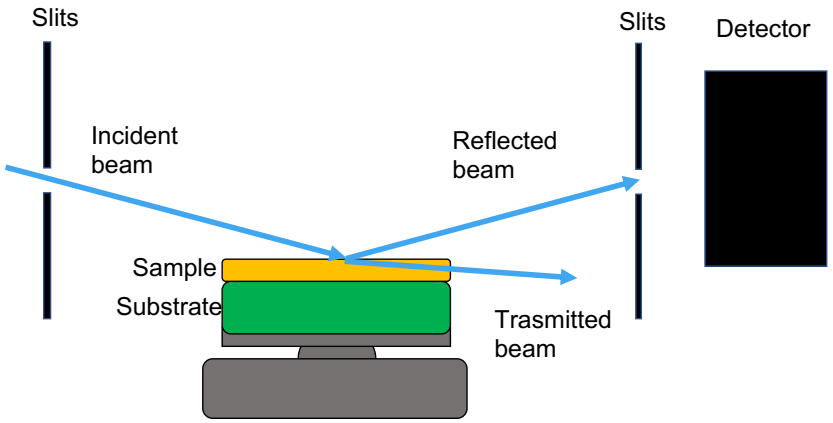

Figure 2.5: Schematic illustration depicting the concept of a neutron-reflectometry experiment. An incident neutron beam (blue) hits a thin sample (yellow) deposited on a substrate (green) at grazing angle θ, and a detector (black) records how many neutrons are reflected. Note that the incident angle θ is heavily exaggerated in the picture, which in reality is between 0.1° - 10°.

In Fig. 2.5, the essential components of the measurement are presented. An incident collimated neutron beam strikes the sample at an angle θ, and part of the beam is reflected and part of the beam is transmitted. The reflected neutrons, together with their respective energies, are registered at the detector. A *beam monitor* registers the flux of the incident beam. However, for the instrument used in the current thesis, CRISP, the incident beam flux was instead determined using an additional measurement: by aiming the beam directly at the detector and measuring the wavelength distribution. The results of these two measurements, one of the incident beam and one of the reflected beam, can then be compared to yield the fraction of reflected neutrons.

Since the variable q_z depends on both the incident angle and wavelength, the reflectivity distribution can be measured by varying θ, λ, or a combination of both [6]. The angles typically range between 0.1° and 10°, and the wavelengths between 2 and 20Å [14, 15]. The choice depends on the neutron-source, and the method differs if the neutron beam is "monochromatic" or "white". For a perfectly monochromatic beam, the neutrons all have identical wavelengths, so the angle θ has to be varied to measure the reflectivity distribution in q_z. If a white beam is used θ can be kept constant, since there is a wide range of different neutron wavelengths in the beam. However, if θ is also varied, an even

wider range in q_z can be achieved. This was done in the present thesis.

To change θ, the sample has to be mounted on a device that can tilt, thereby changing the incident angle of the neutron beam. Furthermore, the slits are required to move accordingly, to collimate the beam at the new angle. Sometimes it is even necessary to change the vertical position of the detector, to account for further angles.

Chapter 3

Method

The experimental method is comprised of two steps: measurement and analysis. The measurement was performed by aiming a collimated neutron beam at an incident angle θ towards the sample and measuring the reflected neutrons. This was then repeated for seven different incident angles, resulting in a broader q_z-spectrum. The data was then reduced, clustered, and analysed. During the reduction phase, undesired data were removed from the data-set. During the clustering phase the remaining data were grouped to form candidate neutron events. In the analysis phase, the candidate neutron events underwent a reflectivity analysis. Ultimately, the reflectivity for all seven incident angles was plotted against q_z, and a fitting procedure was performed to extract information about the sample under study.

3.1 Measurements

The measurements were performed at the ISIS neutron-source facility in England. In the CRISP experiment hall, the Iridum coated Silicon sample were mounted on a tilting platform, and collimators were then adjusted to define the neutron beam. The Multi-Blade was integrated into the CRISP neutron-reflectometry instrument. The data acquisition system was then prepared and the measurement performed.

3.1.1 ISIS

ISIS is a pulsed-neutron source, producing neutron beams via spallation. At the facility, negatively charged hydrogen ions are initially accelerated in a 10 meter long linear accelerator, after which their electrons are stripped away. The resulting protons are sent to a proton synchrotron. In the synchrotron, pulses of protons are created and accelerated to 800 MeV. These proton pulse are then sent to strike a W-target at one of two target

stations, see Fig. 3.9a [16].

The interaction of the proton beam with the W releases spallation neutrons together with other reaction products such as gamma rays. Each collision results in about 15 neutrons, yielding $\sim 10^{13}$ neutrons/s [16]. These neutrons are in the ∼MeV energy range, which is about 6 orders of magnitude greater than the desired cold and thermal energy range. Consequently, the neutrons are moderated by scattering in a 20K liquid H_2 [17], where the neutrons lose energy in each collision. The moderated neutrons are in the ∼meV energy range.

These thermal neutrons are then channelled via beam lines to instruments, see Fig. 3.9b. The instruments are used for neutron experiments, such as diffraction, small angle scattering, imaging and reflectometry, to name a few [16]. One of the reflectometry instruments is CRISP [18], see highlighted red circle in Fig. 3.9b.

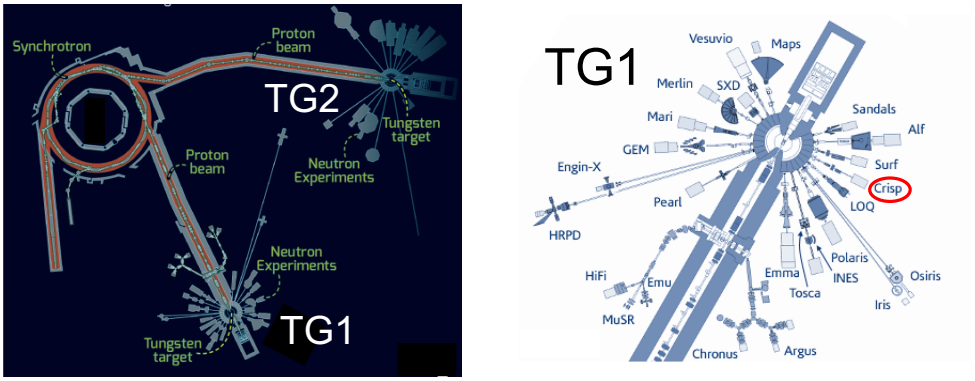

(a) *(b)*

Figure 3.1: A schematic overview of the ISIS Spallation Facility and a close-up of one of the target stations. In (a), a broad overview is shown, presenting the synchrotron ring where the protons are accelerated towards the two different target stations TG1 (bottom) and TG2 (top). The W-target is also seen in each station. In (b), a close up of TG1 is presented, showing all the different experimental halls. The hall where the data for this thesis were collected, CRISP, is highlighted in a red circle. Pictures from Ref. [16], edits by author.

3.1.2 CRISP

CRISP is a horizontal NREF instrument. Thus, the neutron beam is reflected on a sample parallel with the floor of the experimental hall [17]. This configuration allows both solid and liquid samples to be studied. The core features of the instrument are the *chopper*, *sample stand* and the detector. The chopper is "chopping" the received moderated neutron-beam into *bunches*. Then, the sample stand is used to stabilise the sample with anti-vibrational dampening and change the incident angle of the incident beam [17]. Finally, the neutron detector detects the reflected neutrons. In the current configuration, the Multi-Blade was used as the detector.

The setup in the CRISP experimental hall is shown in Fig. 3.2, where a schematic illustration is presented. The 0.5 $\geq$ Å neutrons from the chopper are collimated using slits and directed towards the sample [11]. The Iridium-coated Silicon sample is placed on top of the sample stand, which can be tilted as desired. The Multi-Blade is positioned, and tilted such that the neutrons hit each cassette surface at a 5° incident angle.[1]

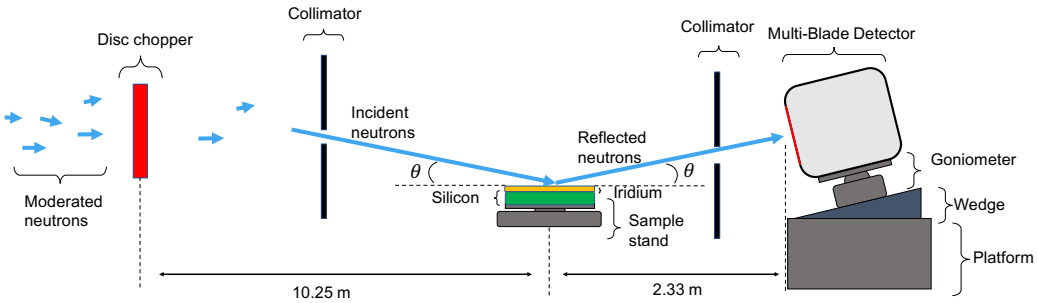

Figure 3.2: Schematic illustration of the experimental setup in the CRISP experimental hall. Moderated neutrons are received and cut into bunches by the chopper. The neutrons are then collimated before and after they hit the sample, followed by detection in the Multi-Blade. A wedge is used to tilt the detector to the desired 5° angle with respect to the neutron beam, and a ganiometer is adopted for fine tuning. Note that the figure is not to scale and that θ (which is between 0.2° - 0.8°) is grossily exaggerated.

The data were collected by varying the incident neutron angle θ on the Iridium sample in Fig. 3.2. The neutron beam reaches the sample at a fixed 1.5°, so to change the incident angle the sample had to be tilted. This was done in seven different angles: 0.2° to 0.8° in steps of 0.1°. Each measurement took ∼6 minutes. Furthermore, since the instrument is to a large extend automated, very few manual adjustments were necessary.

[1] Since the detector was designed to be at a distance of 4 m from the sample, and the experimental distance was 2.33 m, only the first cassette was aligned at the 5° angle to the incident beam, while subsequent cassettes have an angle > 5°. This is because the angular offset between the cassettes designed for 4 m does not correspond to the angular offset required at 2.33 m to keep a consistent incident neutron-beam angle for all cassettes. Consequently, the efficiency for subsequent cassettes will be lower than the efficiency of the first, since the neutron path length in the $^{10}B_4C$-layer will be less for these.

3.1.3 The Multi-Blade

The Multi-Blade is a modular cold- and thermal-neutron detector, designed to fulfil the reflectometry demands at the upcoming spallation source, ESS [11]. Each module is called a *cassette* and acts as an independent Multi Wire Proportional Chamber (MWPC) [19].[2] These cassettes are arranged about a circumference centred at the sample position, and mounted in a gas-filled vessel, see Fig. 3.3a. Each cassette consists of a titanium substrate called a *blade* coated with $^{10}B_4C$, together with a two-dimensional readout-system. The readout-system consists of 32 wires for y-direction, and 32 strips for x-direction. The x and y position is in the detector surface plane, which is defined in Fig. 3.3a. These features can be seen in Fig. 3.3.

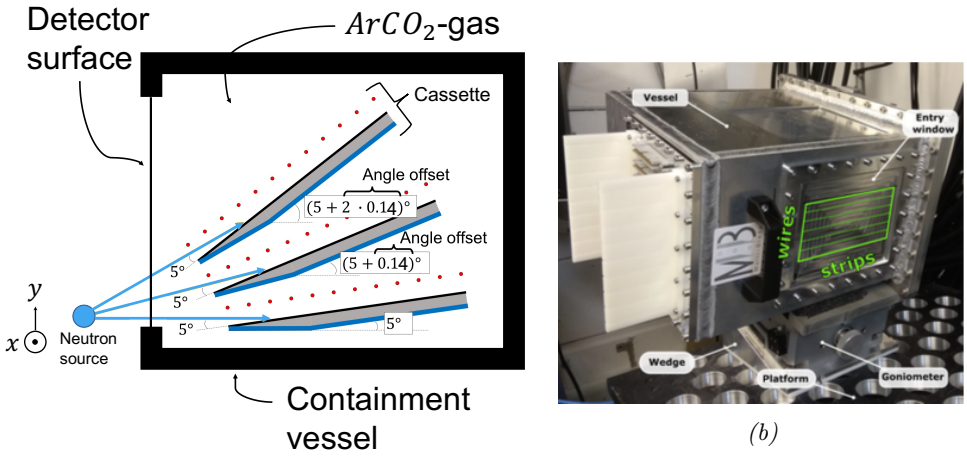

Figure 3.3: In (a) is a schematic illustration of the modular Multi-Blade Detector, showing the $ArCO_2$ gas-filled vessel together with three cassettes. Red circles are wires and dark blue bands strips. The neutron beam strikes each cassette with a 5° incident angle, and a 0.14° angle offset between each cassette exists. In (b) is a picture of the Multi-Blade showing how the strips and wires (green) were oriented in the CRISP instrument environment. (b) from Ref. [11].

The cassettes are MWPCs, which require charged particles or other ionising radiation to register events. Consequently, for the readout-system consisting of wires and strips to detect the neutrons, the neutrons must first be "converted" to charged particles. This

[2] A MWPC detects ionising radiation via an electric field inside a gas chamber. Multiple wires are used as anodes (or cathodes, depending on the polarity of the applied high voltage). When particles move through the gas chamber, they ionise the gas molecules, thereby releasing electrons and positive ions. These freed electrons and ions in turn release more charge via collisions with other gas molecules, resulting in charge avalanches. The electrons (or positive ions) are then collected by wires, and the total collected charge is proportional to the energy of the original ionising particle. From this, the energy of the incident particle is obtained, together with a position, by observing which wires collected the charge [20].

is achieved via a neutron reaction in the $^{10}B_4C$-coating. The neutron capture formulas are:

$$\begin{aligned} {}^{10}\mathrm{B} + \mathrm{n} &\rightarrow {}^{7}\mathrm{Li}^{*} + \alpha \rightarrow {}^{7}\mathrm{Li} + \alpha + \gamma(0.48\,\mathrm{MeV}) + 2.31\,\mathrm{MeV} \quad (94\,\%) \\ {}^{10}\mathrm{B} + \mathrm{n} &\rightarrow {}^{7}\mathrm{Li} + \alpha + 2.79\,\mathrm{MeV} \quad (6\,\%) \end{aligned} \tag{3.1}$$

where the branching ratio is 94% for the first reaction and 6% for the second [1]. The α and ^{7}Li emerge back to back in the centre of momentum frame, allowing only one of the particles to escape the $^{10}B_4C$-coating. The charged reaction product, α or ^{7}Li, is then detected by the wires and strips. The number of wires and strips involved in the detection of an event is denoted *multiplicity*, and is limited by the range of the α or ^{7}Li, see Fig. 3.4. Note that to obtain a two-dimensional reconstruction of the position of a neutron event, two adjacent cassettes are needed. The first cassette uses wires to determine the y-direction, while the cassette above it uses strips for x-direction [11]. This is illustrated in Fig. 3.4.

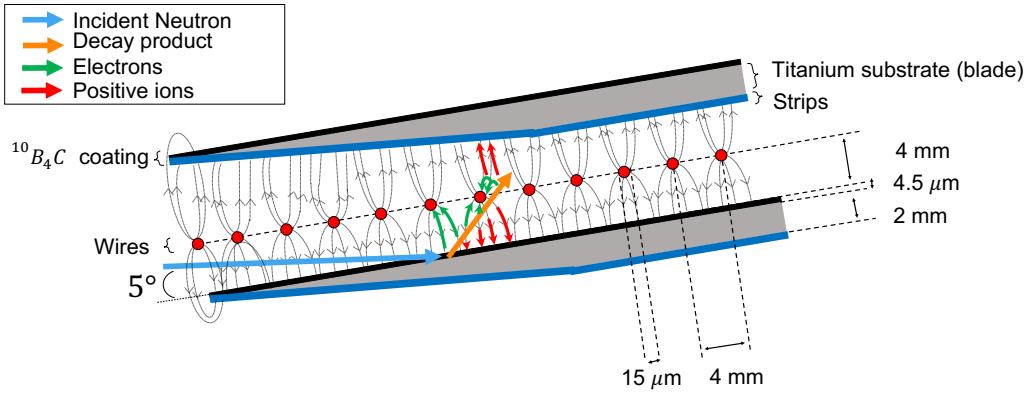

Figure 3.4: Schematic illustration of two adjacent cassettes, where an incident neutron (blue arrow) interacts in the $^{10}B_4C$-coating and a charged neutron product (orange arrow) interacts with the gas. Ionization electrons (green arrows) are collected at the wires, while positive ions (red arrows) are collected at the $^{10}B_4C$-coating or on the strips of the adjacent cassette. Note that the figure is not to scale and that the wire pitch is about three orders of magnitude larger than the wire diameter.

Note the 5° inclination of the cassettes with respect to the incident neutron beam in Fig. 3.3a and 3.4. The inclined geometry, compared to a perpendicular set-up, has three advantages: increased neutron-detection efficiency, increased spatial resolution in the y-direction, and increased counting rate per unit area.

Increased neutron detection-efficiency, results from an increased neutron absorption probability in the $^{10}B_4C$-coating, with an unchanged escape probability for the decay products. The neutron absorption probability is proportional to the distance d travelled through the layer [11], which relates to the width according to:

$$d = \frac{1}{\sin\theta} \cdot w \tag{3.2}$$

where d is neutron travel path, θ the incident angle and w the width of the $^{10}B_4C$-layer. Thus, with an inclination angle of 5°, an 11-fold increase in travel path is acquired compared to the perpendicular setup. Furthermore, since the increased travel distance is a result of traversing the layer at a grazing angle, the maximum escape distance for the decay products remains w. Together, these two effects yield an 11-fold increase in detection efficiency. This because the detection efficiency ϵ is

$$\epsilon \propto P_c \cdot P_e, \tag{3.3}$$

where P_c is the probability of a neutron capture, and P_e is the probability for the decay product to escape the layer. Moving to the inclined geometry, P_c is increased 11-fold. At the same time, P_e is unchanged. This is because the decay product is still emitted in a random direction from the capture reaction, and the maximum escape distance is unchanged.

Increased spatial resolution is obtained from the 5°-projection of the wire plane on the detector surface plane, which gives 11 times finer resolution. This is because, at the frame of reference on the detector surface plane, the wires are 11 times closer together. This is illustrated in Fig. 3.9 in the next Section. Increased counting rate per unit area is a consequence of the projection of the cassette surface on the detector surface, giving an 11 times higher counting rate per unit area. This is because 11 units of area of cassette surface is seen at each unit area at the detector surface. This is a result from the projection. Consequently, if every unit area on the cassette surface has a maximum counting rate of C_{cassette}, this rate will be 11 times higher for every unit area from the perspective of the detector surface according to $C_{\text{surface}} = 11 \cdot C_{\text{cassette}}$.

3.2 Analysis

A schematic outline of the data analysis procedure is shown in Fig. 3.5.

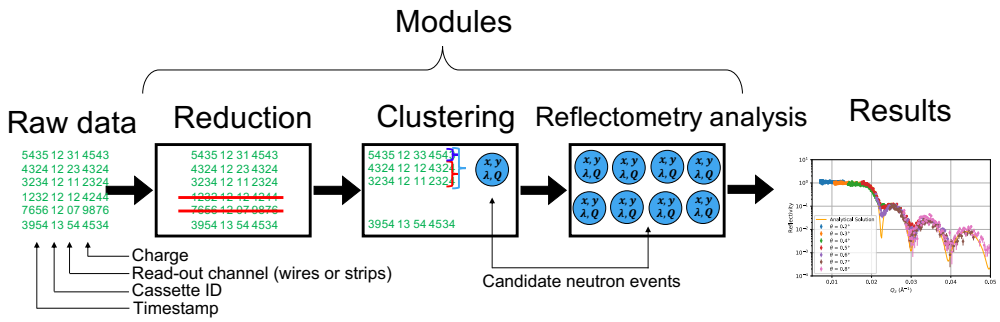

Figure 3.5: Overview of the data processing scheme used in the analysis. The raw data is a text file with measurement data from ISIS. The reduction module removes unwanted data. The clustering module groups the data and forms candidate neutron events, where each candidate neutron event has a (x,y)-position, a wavelength λ_n, and a collected charge Q. The reflectometry analysis-module performs an analysis on the candidate neutrons, producing the final results.

The raw data are in the format of a matrix. Each row represents a data point, and each data point has four columns. The *Timestamp*-column contains the time-of-flight (ToF), which is the time difference between when the neutron bunch passes through the chopper (start signal) and when a signal is registered with the Multi-Blade (stop signal). The *Cassette ID*-column presents the ID number of the cassette that registered the signal, and the *Read-out channel*-column lists which wire or strip was involved. The final column, *Charge*, presents how much charge was collected.[3]

The raw data are first reduced, where a filtering process takes place. The Multi-Blade is designed to detect cold and thermal neutrons. Nevertheless, neutrons of different energies can also be detected, together with other radiations such as X-rays. Therefore, a cut is performed: events outside the designated cold and thermal neutron energy range are discarded.

After the reduction module, the filtered data are sent to the clustering module, where the reduced data are processed to identify candidate neutron events. This is done by inspecting which data are correlated both in time and position, and then grouping them together to form a candidate events. The candidate events are then sent to the reflectometry-analysis module. The analysis is done by examining data from reflected neutrons and

[3]Note that the collected charge is not related to the energy of the neutron involved in the event. Instead, the charge represents the energy of the detected product, ^{7}Li or α, from the neutron capture process in the $^{10}B_4C$-layer (recall Eq. (3.1)). If more than one wire and strip were involved in the event, the charge distribution can be used to pinpoint more exactly where the neutron hit the surface, since this is related to the position of the decay product. This is done via a center-of-gravity (CoG) calculation on the collected charge of all wires and strips involved.

from incident neutrons. It is possible to calculate the reflectivity as a function of q_z. This results in a profile for reflectivity as a function of q_z, which is then fitted to obtain material properties such as thickness and roughness.

3.2.1 Reduction

The Multi-Blade is a cold and thermal neutron detector. Unfortunately, the beam used in the measurements was a white beam, containing a large range of neutron energies. Although high-energy neutrons are unlikely to be directly detected, they can thermalise within the detector through scattering in the substrate, and subsequently be detected. The recorded coordinate will then not be accurate, since the neutron has scattered from its initial hit position. Consequently, it would be preferable to remove data due to events that did not originate from cold and thermal neutrons.

Although not all the undesirable events can be removed with certainty, there is a large subset that can be directly discarded. This is done by studying the time stamp of the data, since this gives information about the neutron kinetic energy through:

$$E_n = \frac{m_n v^2}{2} = \frac{m_n}{2}(\frac{L}{\text{ToF}})^2 \Leftrightarrow \text{ToF} = \sqrt{\frac{m_n \cdot L^2}{2E_n}}. \tag{3.4}$$

where m_n is the neutron mass, v the neutron velocity, L the neutron flight distance, and ToF the neutron time-of-flight [1]. L corresponds to the length between chopper and detector (12.58 m), and ToF the flight time of neutron between chopper and detector (that is, the time stamp). Inserting the desired energy limits in Eq. (3.4) allows for a threshold on time stamp to be set. All data outside this range are discarded, since they do not belong in the cold and thermal energy range. That is, a cut is performed so that only data with a ToF corresponding to an energy-range 2 meV $\leqslant E_n \leqslant$ 25 meV are retained. The resulting reduction is clearly demonstrated in Fig. 3.6a.

Concerning collected charge Q, a lower limit is determined by the background noise. This is determined from a measurement of Q when no beam was incident on the detector surface. Below this Q-value, a neutron event cannot be discerned from noise, and thus data under this limit are discarded. The Q-value threshold was set to 3500 QDC channels. The resulting reduction is seen in Fig. 3.6b.

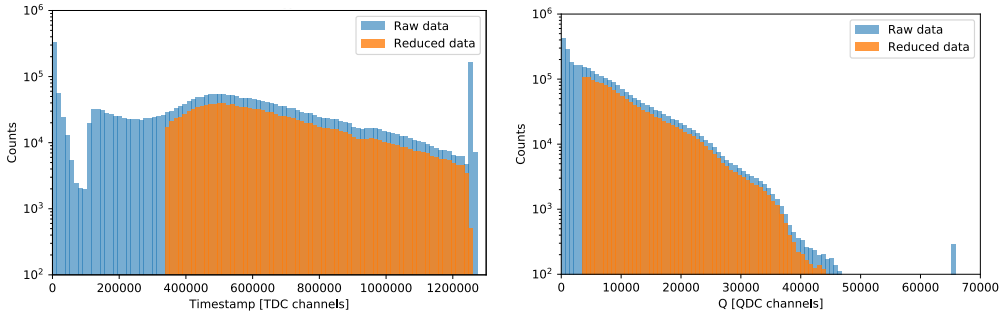

(a) *(b)*

Figure 3.6: Comparison between raw data (blue) and reduced data (orange). In (a), histograms of the time stamp for raw and reduced data are presented together for comparison, while in (b) histograms of collected charge are presented before and after the cut. Note that for both plots the amount of reduced data is slightly less than the raw data over the entire spectrum. This is because both cuts for reduction were performed simultaneously.

3.2.2 Clustering

Candidate neutron events are created by grouping related data from the reduced data set together in clusters. The geometry of the Multi-Blade defines what a cluster should contain. Since the neutron capture fragment is required to pass the wire plane to be detected by the strips, a candidate neutron event should have one of two possible configurations. Let N_w and N_s be the maximum multiplicity for wires and strips, respectively. The configurations are then:

- 1 to N_w data points from adjacent wires + 1 to N_s data points from adjacent strips
- 1 to N_w data points from adjacent wires

The first configuration corresponds to an event where the neutron capture fragment had sufficient energy to pass the wire plane, hence permitting positive ions to be collected by the strips (recall Fig. 3.4). The second configuration belongs to an event where the fragment did not pass the wire plane. There are also conditions on allowed time stamps for the data points contained in a cluster. The data points are acquired from signals sent by the Multi-Blade, which originate from the neutron-capture fragment moving at a finite speed through the MWPC. The fragment requires time to generate the ionization, and the released charge takes time to be collected by the wires and strips. Therefore, there is a certain time range that determines which data points can be related. This time is labelled ΔT and is defined as the maximum time difference between the first *wire signal* and the last *strip signal* for a single neutron event, i.e. the time it takes for a neutron event to be fully registered. Furthermore, since a capture fragments must pass the wire plane before it can reach the strip plane, the first signal from the wires in the cluster must occur before the first signal from the strips (recall Fig. 3.4).

The clustering method is divided into three steps: Time clustering, Spatial clustering and Final clustering. The process is illustrated in Fig. 3.7.

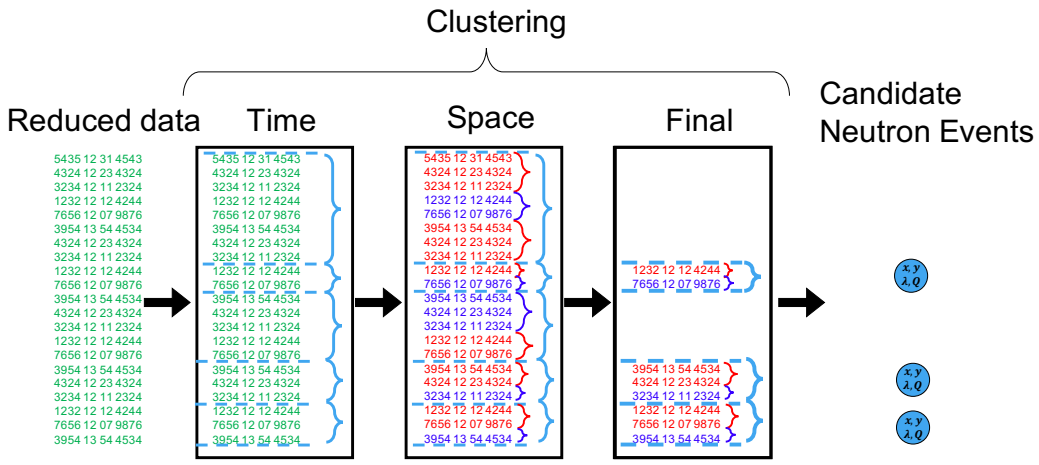

Figure 3.7: Overview of the clustering method used to process the reduced data to identify candidate neutron events. The first step is the Time clustering module, which groups data points within a predefined ΔT. These data points are then passed to the Spatial cluster module, which groups the data points based on spatial location. Here, red numbers represent adjacent wires, and blue numbers represent adjacent strips. In the Final clustering module, all nonviable clusters are discarded, producing a set of candidate neutron events represented as blue circles.

Time clustering

The first step is Time clustering, which involves sorting through the data set and group data points with time stamps within ΔT of one another, see Fig. 3.7. The data points contained the time clusters are to a first approximation obtained from the same neutron event, and are used as the basis for the creation of candidate neutron events.

ΔT is set to correspond to time difference between the first signal from the wires and the last signal from the strips, which is in the order of μs. This is time it takes for the neutron event to be registered. However, in reality this is not a constant, but a distribution. Sometimes the time is shorter, and sometimes the time longer. This is because the time it takes to form a neutron event depends on how the reaction product is ejected out of the $^{10}B_4C$-layer, which is random. If it is ejected perpendicular to the surface, it will quickly pass the wire plane and allow charge to be collected by the strips, thereby forming a neutron event. In contrast, if the decay product is ejected at an angle it will have to travel a longer distance before it passes the wire plane. The time ΔT can consequently not be known beforehand, but varies from event to event. Therefore, the ΔT used in the algorithm is assigned an intermediate value, working for a majority of neutron events.

The limits placed on ΔT are well defined by the detector. A minimum and maximum time results from the minimum and maximum energy of the neutron capture fragments, the distance between the strips and the wires, and the voltage applied in the detector. All these factors contribute to how long it takes for the decay product to traverse the wire plane, and then to have their released charge collected. To find an appropriate value for ΔT, statistics from the measurements are studied. An illustration of the investigation can be seen in Fig. 3.8. At ~ 6 μs an appropriate value for ΔT is found (vertical dashed line), which gives the maximum percentage of usable clusters (those containing one wire spatial cluster and one strip spatial cluster, or only one wire spatial cluster) and low percentage of unusable clusters (only one strip spatial cluster, and clusters containing several wire and strip spatial clusters). Note the dramatic drop in useful clusters at ~ 7 μs, this corresponds to when ΔT is made large enough to make it statistically likely for the cluster to contain data from two consecutive neutron events.

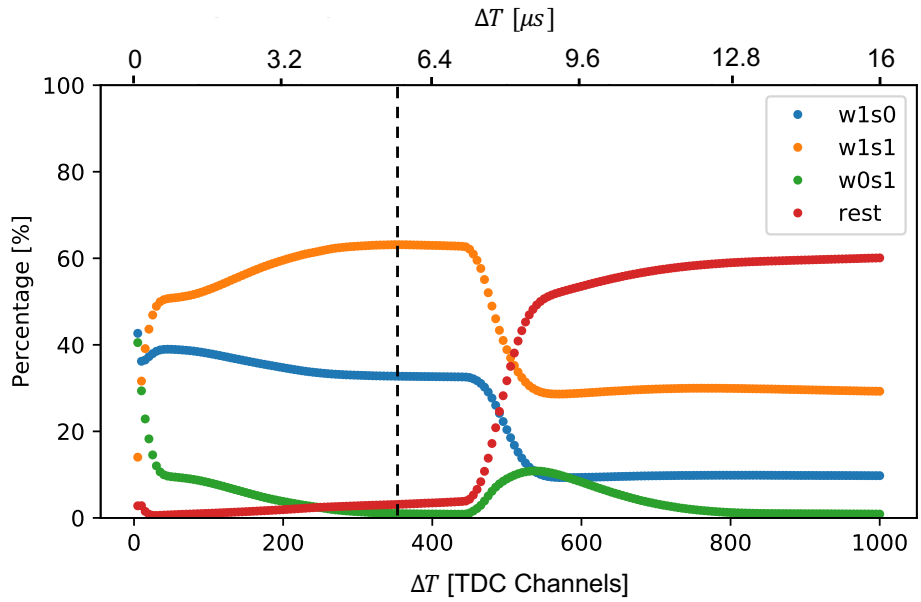

Figure 3.8: Plot demonstrating how to find the best value for ΔT. The percentage of different types of clusters as a function of ΔT is presented, where wNsM denotes a cluster with N wire spatial clusters and M strip spatial clusters. The interesting clusters here are the orange (one wire spatial cluster and one strip spatial cluster) and the blue (one wire spatial cluster). Between around 5 and 7 μs a plateau is seen, followed by a dramatic percentage drop in the useful clusters.

Spatial clustering

Spatial clustering is the process of identifying which data originate from adjacent wires or adjacent strips within a Time cluster, see Fig. 3.7. By grouping the data into Spatial clusters, it is possible to obtain a hit position for the candidate event. In the CRISP-

configuration, the wires of the Multi-Blade give y-position and strips give x-position, where x and y refer to the detector surface plane.

The y-coordinate is determined by performing a center-of-gravity (CoG) calculation on the wire coordinates within the Spatial-cluster according to:

$$\text{CoG} = \frac{\sum_{i=0}^{n} Q_i y_i}{\sum_{i=0}^{n} Q_i} \tag{3.5}$$

where n is the number of data points within the wire Spatial cluster, Q_i is the charge collected in the i:th data point, and y_i is the wire coordinate of the i:th data point.

For the hit position, the x- and y-coordinate must be calculated using slightly different methods. The wire coordinate is calculated according to:

$$y_i = p \cdot \sin(5^\circ + \text{A}_{\text{offset}}) \cdot \text{wireNbr} + \text{S}_{\text{offset}} \tag{3.6}$$

where p is the wire pitch (4 mm), wireNbr is the wire of the recorded event, A_{offset} and S_{offset} are the angular and spatial offset of the cassette that recorded the event, respectively (recall Fig. 3.3a). The x-coordinate is obtained using the same center-of-gravity calculation as for y. However, to obtain the strip coordinates, the following formula is used:

$$x_i = p/2 + p \cdot \text{stripNbr} \tag{3.7}$$

where stripNbr is the strip that recorded the event. The calculation for x differs from y because there is no projection involved for the strips. This concept is illustrated in Fig. 3.9.

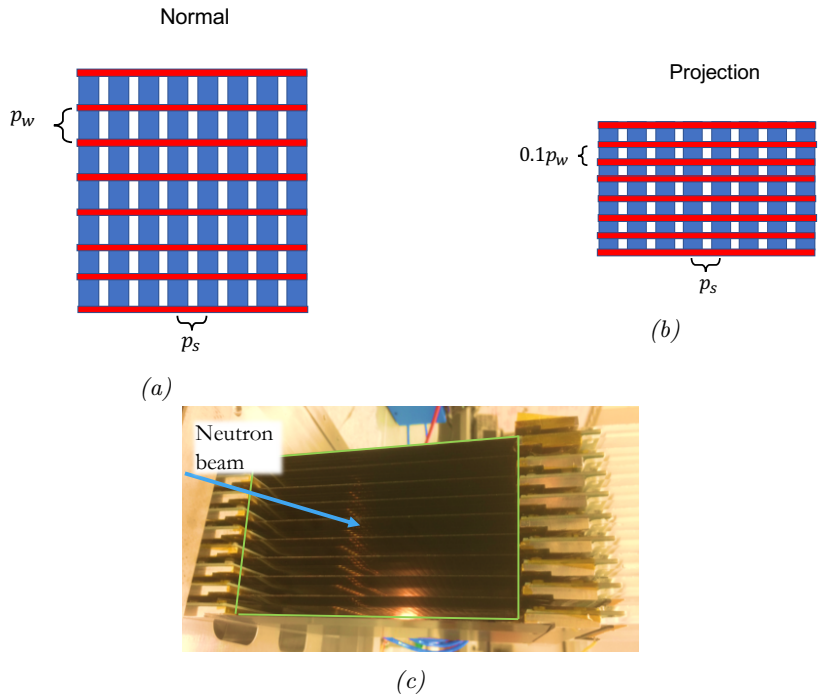

Figure 3.9: Illustration presenting the projection of the cassettes on the detector surface, where red lines represent wires and blue lines represent the strips. In (a), the plane of the cassette lies with the page, while in (b) the projection on the detection plane is seen. In the projection, the distance between the strips p_s is unaffected, but the distance between the wires p_w is only 10% of the perpendicular distance. In (c) a picture of nine adjacent cassettes are shown together, further illustrating the projection effect. (c) from Ref. [11].

Final clustering

After the Time and Spatial clustering is performed, a set of *Pre clusters* are obtained. To determine which of these could correspond to a neutron event, the distribution of the spatial cluster contents in the Pre clusters are examined. This is presented in Fig. 3.10.

A candidate neutron event can contain only two possible configurations:

- 1 wire spatial cluster + 1 strip spatial cluster
- 1 wire spatial cluster

In the figure it is seen that a majority of the Pre clusters, 63.08% + 32.73% = 95.81%, are clusters expected from the geometry of the Multi-Blade. These are emphasised with red lines. The rest are Pre clusters, which have only one strip spatial cluster, 0.94%, or higher multiples of wire and strip spatial clusters, 3.25%. The first alternative

is unfeasible, since the decay product must first pass the wire plane before it can be registered at the strips (recall Fig. 3.4). These Pre clusters are thus discarded. The other combinations could be a result of multiple neutron events within a time span $< \Delta T$.[4] That would imply that data from more than one neutron event is contained in a single Pre cluster. Unfortunately, these Pre clusters cannot be used, since it is unclear which wire and strip spatial cluster pair up to form a candidate neutron event. These are consequently also discarded.

Using the acceptable Pre clusters, the neutron energy is found by using the ToF from the first wire event in the each Pre cluster (since this is the best approximation of when the neutron first reached the detector) and inserting in Eq. (3.4). From this, the identification of the candidate neutron events is finalised, and they are labeled with the information (λ_n, (x,y)) or (λ_n, x). For standard neutron reflectometry, only λ_n and x are required, so both types of clusters are utilised in the reflectometry analysis.

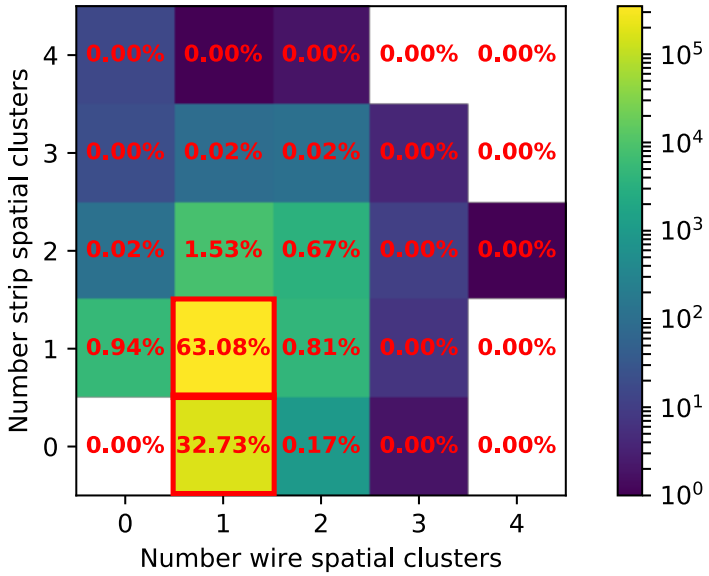

Figure 3.10: Histogram of the distribution of number of spatial clusters within a given Pre cluster. The numbers given in the grid represents the percentage of that particular combination of wire and strip spatial clusters, while the colour bar to the right shows the absolute numbers (note the logarithmic scale). Furthermore, the percentage is rounded to two decimal places, so several tiles may have different colours but the same percentage. The Pre clusters that can be utilised in the current algorithm are emphasised with red lines.

[4] They could also be a result from electronic noise that was not filtered by the reduction. Another reason could be interference from other particles. This could be X-rays, or fast neutrons that thermalised within the detector.

3.2.3 Reflectometry

As discussed in Chapter 2, reflectometry is the study of the fraction of reflected neutrons for a specific wavelength λ_n and incident angle θ. Therefore, knowledge of both the incident flux and reflected flux are crucial. In the present thesis, two data sets are analysed: one from reflected neutrons (with seven different incident angles), and one from the direct beam, measuring the incident flux.

Both data sets are processed using the clustering method, resulting in candidate neutron events. These candidate neutron events are then used to produce histograms of the wavelength λ_n of the incident and reflected neutrons. However, since the irradiation times were different for the different measurements, the histograms require normalisation. The normalisation is performed by using the number of bunches acquired. That is, "packets" of neutrons received from the chopper. This is because the number of bunches is related to the irradiation time. A schematic illustration of the resulting normalised histograms for wavelength λ_n is seen in Fig. 3.11.

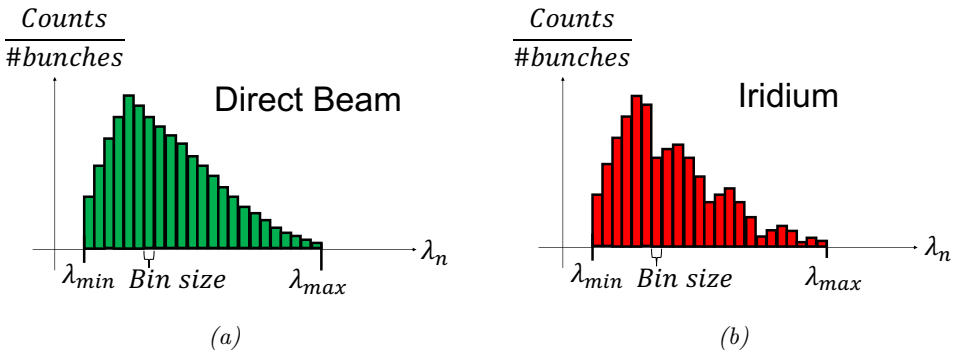

Figure 3.11: Schematic illustration of the normalised histograms of neutron wavelength λ_n. In (a), the Direct Beam data are seen (green), while in (b) and normalised Iridium data are presented (red). The illustrated structure in the Iridum data results from interference between the reflected neutron waves. This is not present in the Direct Beam since no reflection was involved. Both histograms have the same range and bin size, and the bin centres are used as wavelength for the analysis. Note that the bin size is heavily exaggerated in this illustration.

The bin size (0.012 Å) and range (1.7 Å to 6.3 Å) of the two histograms must be equal to facilitate an accurate comparison between the two spectra. The final step is to iterate through each bin, using the bin centres for wavelength, and comparing the number of counts in the Iridium and Direct Beam data. From this, the fraction of reflected neutrons for a given wavelength is obtained using:

$$R = \frac{\mathrm{Ir_{norm}}}{\mathrm{DB_{norm}}}\Big|_{\lambda_{\mathrm{bin\ centre}}} \tag{3.8}$$

where $\mathrm{Ir_{norm}}$ and $\mathrm{DB_{norm}}$ are the normalised Iridium and Direct Beam data, respectively.

This is then plotted against q_z, recall Eq. (2.1). This procedure is repeated for each of the seven data sets from Iridium, one from each recorded angle θ, which are then plotted together to establish a wide range in q_z.

When this is completed, an overall normalisation, based on the q_z region of total reflection, is implemented to further improve the results. From the initial results a plateau corresponding to the region of total reflection is easily identified. This is set to 1. By performing the normalisation in the plateau region, and applying this normalisation at the overlap from data from each θ, a reliable normalisation for the aggregated spectrum is determined.

Using the theory for a thin film on a substrate presented in Chapter 2, an analytical function, see Eq. (2.14), for the reflectivity profile was implemented in Python. The function depended on five parameters: the scattering length density of Iridium and Silicon $\mathrm{Nb}_{\mathrm{Ir}}$ and $\mathrm{Nb}_{\mathrm{Si}}$, the roughness between the interfaces σ_{AirIr} and σ_{IrSi}, and the Iridium thickness Δ_{Ir}. This function was then fitted to the data using the SciPy function *scipy.optimize.curve_fit* [21].

Chapter 4

Results

The result from the reflectometry analysis on the Iridium sample is presented together with a fitted function in Fig. 4.1.

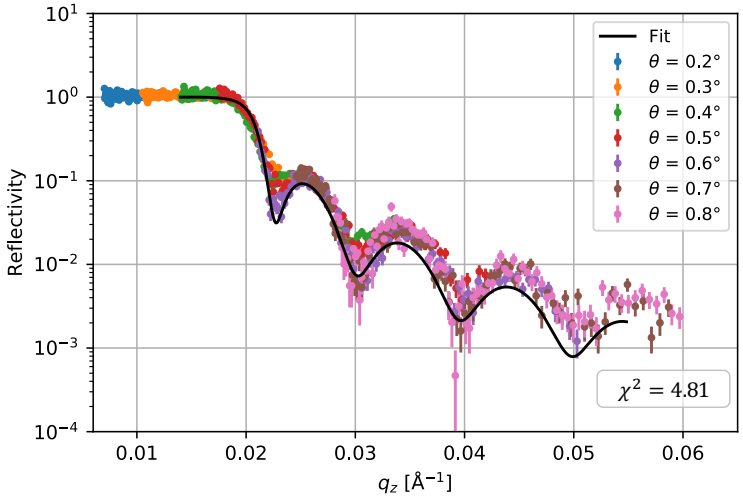

Figure 4.1: Fraction of reflected neutrons as a function of momentum transfer q_z perpendicular to the interface. The colours correspond to different angles of incidence for the neutron beam. For q_z between 0.0075 Å^{-1} and 0.018 Å^{-1}, total reflection is observed, while for $q_z > 0.018$ Å^{-1} there is a decrease in reflectivity modulated by a fringe pattern. The fringes result from interference between neutron waves reflected at the Iridium surface and the Si surface, while the decrease results from the diminishing probability of reflection. In the errorbars the statistical uncertainties are shown.

Left of 0.018 $Å^{-1}$, the expected region of total reflection is clearly seen. To the right of 0.018 $Å^{-1}$, there is the fringe modulated decline, as predicted from theory. The measurements for the seven different angles overlap nicely. A fit is presented together with the data, which, by allowing all five parameters to vary, resulted in the following parameters:

	Nb_{Ir}	Nb_{Si}	σ_{AirIr}	σ_{IrSi}	Δ_{Ir}
Value	7.66e-6 $Å^{-2}$	5.25e-6 $Å^{-2}$	4.46e-7 Å	1.4e-7 Å	550 Å
Uncertainty	±2.57e-8 $Å^{-2}$	±1.53e-8 $Å^{-2}$	±1.92e-7	±0.00 Å	±2.75 Å

Table 4.1: Fit parameters corresponding to a goodness of fit value $\chi^2 = 4.81$.

where Nb_{Ir} is the SLD of Iridium, Nb_{Si} is the SLD of Silicon, σ_{AirIr} is the roughness at the Air-Ir interface, σ_{IrSi} the roughness at the Ir-Si interface, and Δ_{Ir} the thickness of the Iridium layer. Appropriate starting values for the fitting procedure was established to get this result. This was done using knowledge about how the parameters corresponded the critical edge and the distance between the fringes. Using Eq. (2.8), Nb_{Si} was found to be $\approx$ 2e-6 $Å^{-2}$. Additionally, using Eq. (2.15), a starting value for Δ_{Ir} was found to be $\Delta_{Ir} \approx 600$Å.

The fit obtained a goodness of fit value equal to $\chi^2 = 4.81$. Note that the values for the roughnesses σ_{AirIr} and σ_{IrSi} are below subatomic scales ($< 10^{-15}$ m) and can effectively be regarded as zero. It was previously known that the thickness of the Iridium sample was ∼550 Å, which is in good agreement with the 550 ± 2.75 Å result from the fit. The uncertainty in percentage is ± 0.55%.

The SLD of Iridium, Nb_{Ir}, was found to be 7.66e-6 $Å^{-2}$ ± 2.57e-8 $Å^{-2}$. This is close, within ± 2.8%, to the calculated value of 7.45e-6 $Å^{-2}$ [22]. The discrepancy could depend on an inaccurate estimate of the errors. From the data set used to perform the reflectometry analysis there was no calculation of the systematic errors. This is because the relevant parameters needed to calculate the systematic uncertainties were unavailable. Consequently, only the statistical uncertainties could be included in the current thesis.

4.1 Outlook

There are two main areas in the current data-processing method that can be improved: the clustering module and the reflectometry module. The clustering module can be improved to incorporate more data than is presently being used in the analysis. The reflectometry module can be improved to produce a more accurate result by using a more advanced analysis algorithm. This would use the high spatial resolution of the Multi-Blade detector to get a more precise estimate of the incident angle θ.

4.1.1 Clustering

With the current clustering algorithm 96% of the data can be used. Methods to further develop the algorithm, enabling it to utilise the remaining 4%, are nevertheless desirable. The main issue is that the actual length in time of an event is not known, so an intermediate value ΔT is used to group all candidate neutron events. Consequently, sometimes data from more than one neutron event are contained in a single cluster, and sometimes a neutron event is divided across more than one cluster. A more sophisticated method of identifying which data points are associated with a specific neutron event is thus required. One method of achieving this would be to examine the collected charge in the useful clusters obtained from the current algorithm. From this information, it could be possible to discern which wire and spatial clusters are related.

One discriminator is the charge ratio between wires and strips within the same candidate neutron event, see Fig. 4.2. The seven most probable multiplicity combinations are presented, where it is clearly seen that their distributions differ in their charge ratio.

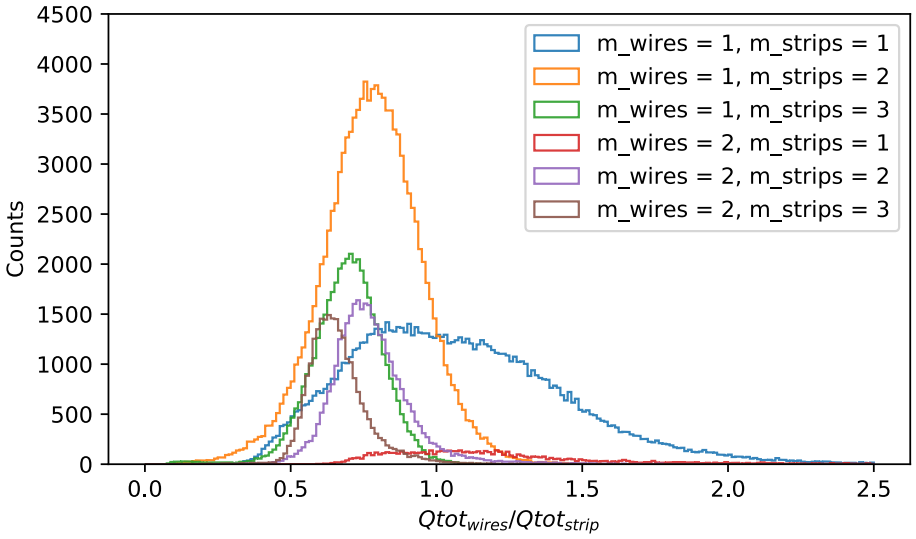

Figure 4.2: Histogram of Qtot-wires/Qtot-strips for different combinations of multiplicities m from the candidate neutron events obtained with the current clustering algorithm. See the legend for the colour coding.

These distributions present the relationship between charge collected in strips and wires in the same neutron event. Consequently, they provide unique "finger prints" of neutron events with specific multiplicity combinations. In a Pre cluster with several different wire and strip spatial clusters (recall Fig. 3.10), this can therefore be used to pair up which spatial clusters are correlated.

These features are statistical in nature, with significant overlaps between many of the distributions. Consequently, this could be used to identify neutron events, but it would be necessary to assign the created candidate events a probability. This would be done in the following manner. Take two spatial clusters, one wire and one strip spatial cluster, in a Pre cluster with several of each, and calculate their charge fraction. Compare this fraction to the distribution related to their specific multiplicity combination, and calculate how likely it would be to get the obtained charge fraction. From this a probability is acquired, representing how likely the wire and strip spatial clusters are correlated to an actual neutron event of this multiplicity combination. This mathematical method is a *hypothesis test* and is rigorously described in Ref. [23].

The resulting probability is labelled *quality factor*, and is a measure of how probable it is that the spatial clusters were correctly clustered. Using the quality factor, it would not only be possible to obtain more data, but it would be possible to get an approximation of the quality of the data. In this fashion, it would possible to decide between utilising a large data set with poorer quality, or a smaller one with excellent quality. This would be done by applying limits, such as only keeping events which fall within one standard deviation around the mean in their distributions.

The distributions can also be used to see which spatial clusters are not a result from a neutron event. For example, a typical neutron event produce about three orders of magnitude more primary charge in the Multi-Blade than a typical X-ray [11]. As an illustration, assume a Pre cluster has been created with a wire spatial cluster from a neutron event and a strip spatial cluster from an X-ray event. If the fraction of charge would be calculated, the ratio would be very off. It would not fit in the distribution in Fig. 4.2. It could therefore with a very high statistical certainty be discarded that these spatial clusters are created from a single neutron event.

4.1.2 Reflectometry

A feature in Fig. 4.1 is that the fringes from the data are not very prominent. This is an effect from setting θ to the measured reflected angle in the experimental setup (recall Fig. 3.2). This assumes a perfectly collimated beam, consequently ignoring the width and divergence of the beam. This results in an uncertainty when calculating q_z. If instead the hit coordinate on the detector would be used to reconstruct the actual θ value on an event-by-event basis, a more accurate q_z could be identified. This would result in a clearer fringe pattern. This could be achieved by using the y-coordinate from the neutron events to see where on the detector the neutron struck. By combining this number with the detector-to-sample distance (recall Fig. 3.2), the angle θ can be calculated, and consequently q_z.

Since the Multi-Blade is designed to have an unprecedented spatial resolution in one direction, this makes the θ-correction technique ideal for the Multi-Blade. Using its fine resolution, a highly accurate measurement of y, and consequently θ and q_z, is obtained. This has recently been tested successfully [14].

4.2 Conclusion

All the relevant charactheristics from the NREF experiment can clearly be seen in Fig. 4.1, showing that the detector is working as expected. Furthermore, the thickness of the Iridium was correctly identified as 550 Å, with a parameter value $\Delta_{\mathrm{Ir}} = 550 \pm 2.75$ Å. The SLD of Iridium was close to that of the found parameter value, with a discrepancy of 2.8%. The difference could be due to an inadequate estimation of the measurement errors. The method can be further improved by using the high spatial resolution of the Multi-Blade. This would result in a clearer fringe pattern and a more accurate estimation of the fitting parameters. Furthermore, by further improving the clustering algorithm more of the data can be utilised, hence permitting better statistics. Nevertheless, the results clearly demonstrates the excellent functionality of the Multi-Blade detector.

References

[1] K.S. Krane. *Introductory Nuclear Physics*. Wiley, 1987. ISBN 9780471805533. URL https://books.google.se/books?id=ConwAAAAMAAJ.

[2] Robert Cubitt and Giovanna Fragneto. Neutron reflection: Principles and examples of applications. In E.R. Pike and P.C. Sabatier, editors, *Scattering, Two-Volume Set: Scattering and inverse scattering in Pure and Applied Science*, chapter 2.8.3, pages 1998–2008. Elsevier Science, 2001. ISBN 9780080540733. URL https://books.google.se/books?id=zlBRWqo39QgC.

[3] R. Pynn. Neutron scattering—a non-destructive microscope for seeing inside matter. In H. Schober L. Liyuan, R. Rinaldil, editor, *Neutron Applications in Earth, Energy and Environmental Sciences*, chapter 2, pages 15–36. Springer US, 2009. ISBN 9780387094151.

[4] J. Penfold and R. K. Thomas. The application of the specular reflection of neutrons to the study of surfaces and interfaces. *Journal of Physics: Condensed Matter*, 2, 1990.

[5] J.R.P.Webster. Introduction to neutron reflectivity. URL https://www.isis.stfc.ac.uk/Pages/neutron-reflectivity---introduction12224.pdf.

[6] IAEA. Summary. In *Neutron Reflectometry: A probe for materials surfaces*, pages 1–29. International Atomic Energy Agency, Vienna, 2006. ISBN 9201039069.

[7] Mary H. Wood and Stuart M. Clarke. Neutron reflectometry for studying corrosion and corrosion inhibition. *Metals*, 7(8), 2017. ISSN 2075-4701. doi: 10.3390/met7080304. URL http://www.mdpi.com/2075-4701/7/8/304.

[8] J. Stahn and A. Glavic. Focusing neutron reflectometry: Implementation and experience on the tof-reflectometer amor. *Nuclear Instruments and Methods in Physics Research Section A: Accelerators, Spectrometers, Detectors and Associated Equipment*, 821:44 – 54, 2016. ISSN 0168-9002. doi: https://doi.org/10.1016/j.nima.2016.03.007. URL http://www.sciencedirect.com/science/article/pii/S0168900216300250.

[9] European Spallation Source. ESS. URL https://europeanspallationsource.se/.

[10] F Piscitelli et. al. Study of a high spatial resolution 10 b -based thermal neutron detector for application in neutron reflectometry: the multi-blade prototype. *Journal of Instrumentation*, 9(03):P03007, 2014. URL http://stacks.iop.org/1748-0221/9/i=03/a=P03007.

[11] F. Piscitelli et. al. The multi-blade boron-10-based neutron detector for high intensity neutron reflectometry at ess. *Journal of Instrumentation*, 12(03):P03013, 2017. URL http://stacks.iop.org/1748-0221/12/i=03/a=P03013.

[12] ESS. FREIA, . URL https://europeanspallationsource.se/instruments/freia.

[13] ESS. ESTIA, . URL https://europeanspallationsource.se/instruments/estia.

[14] G. Mauri et. al. Neutron reflectometry with the multi-blade 10b-based detector. 2018. URL https://arxiv.org/abs/1804.03962.

[15] Z. Tun. Design of a neutron reflectometer at a research reactor. In *Neutron Reflectometry: A probe for materials surfaces*, pages 59–67. International Atomic Energy Agency, Vienna, 2006. ISBN 9201039069.

[16] Science Technology Facilities Council. Isis neutron and muon source, . URL https://www.isis.stfc.ac.uk/Pages/home.aspx.

[17] S. Langridge C.J. Kinane, R.M. Dalgliesh and D.G. Bucknall. Crisp instrument manual. URL https://www.isis.stfc.ac.uk/Pages/crisp-instrument-manual-nov-2010.pdf.

[18] Science Technology Facilities Council. Crisp, . URL https://www.isis.stfc.ac.uk/Pages/Crisp.aspx.

[19] G. Charpak. Electronic imaging of ionizing radiation with limited avalanches. *Nobel Lecture*, 1992. URL https://www.nobelprize.org/nobel_prizes/physics/laureates/1992/charpak-lecture.pdf.

[20] W.R. Leo. *Techniques for Nuclear and Particle Physics Experiments: A How-to Approach*. Springer Berlin Heidelberg, 2012. ISBN 9783642579202. URL https://books.google.se/books?id=yc4qBAAAQBAJ.

[21] The Scipy community. scipy.optimize.curve_fit. URL https://docs.scipy.org/doc/scipy/reference/generated/scipy.optimize.curve_fit.html.

[22] P. Kienzle. Neutron activation and scattering calculator. URL https://www.ncnr.nist.gov/resources/activation/.

[23] Enger J. Englund G. Grandell J. Holst L. Blom, G. *Sannolikhetslära och statistikteori med tillämpningar*. Studentlitteratur AB, 2016. ISBN 9789144123561.

The project reported on in this thesis
was performed by

The Multi-Blade Group

in collaboration with

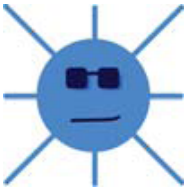

The Source-based Neutron Irradiation Group of the
Division of Nuclear Physics at Lund University

and

The Detector Group of the European Spallation Source ERIC

with support from

The Horizon 2020 BrightnESS Project, Proposal ID 676548